Robotics and Computer–Integrated Manufacturing 73 (2022) 102221

Contents lists available at ScienceDirect

Robotics and Computer-Integrated Manufacturing

journal homepage: www.elsevier.com/locate/rcim

Hand-eye calibration for 2D laser profile scanners using straight edges of common objects

Jing Xu [a], Jian Li Hoo [a], Stylianos Dritsas [b,*], Javier Gomez Fernandez [a]

[a] Engineering Product Development, Singapore University of Technology and Design Singapore 487372, Singapore
[b] Architecture and Sustainable Design, Singapore University of Technology and Design Singapore 487372, Singapore

ARTICLE INFO

Keywords:
Robot-based 3D scanning system
Hand-eye calibration
Laser line scanner

ABSTRACT

This paper presents a method for calibrating a 2D profile laser scanner mounted on an industrial articulated robot; a task also known as the hand-eye calibration problem. The challenge of recovering the transformation matrix, from the robot's flange coordinate system to the scanner's coordinate system, lies in the lack of sufficient 3D information, as only 2D data is available. The task is typically performed using precision calibration specimens such as spheres, disks, and planes or using additional external devices such as cameras and 3D sensors. Here, we present an approach based on detecting straight edges found in common objects. Points extracted from the same edge, under various robot poses, are used to solve the calibration problem using a two-phase least-squares strategy, where rotation is recovered first, followed by translation. The process is semi-autonomous, requires minimal laborious and error-prone manual operations; its setup effort is small, because common objects can be used instead of costly precision gauges or external devices; it does not require large number of samples and it is simple to reason about, implement and compute.

1. Introduction

As computer vision sensors became progressively affordable over the past decades, their application increased in manufacturing and industrial quality control. Indicative examples include inspection of airplane engine blades [1], detection of surface abnormalities on machined components [2], robot grinding of aviation and turbine blades [3], robot-assisted medical applications [4], reverse engineering objects to CAD models [5], and automatic robot navigation [6-8].

The work presented here focuses on a subset of computer vision sensors, namely 2D profile scanners. They acquire series of points $p_s : [x_s, 0, z_s]$, where x_s is the horizontal and z_s is the depth coordinates with respect to the sensor's scanning plane. Applications include measuring linear dimensions, verifying heights, and comparing designed versus manufactured objects [9-11]. Mounting profile scanners on positioning equipment allows for 3D shape reconstruction once the scanner and positioner are coordinated.

Integration of computer vision with positioning equipment, such as an articulated industrial robot arm (see Fig. 1), requires performing a process known as hand-eye calibration [12]. Its objective is to determine the transformation matrix between the robot's flange coordinate system (F_b) and the scanner's vision coordinate system (Fs), such that data acquired from different poses, robot positions and orientations, may be registered against a common 3D coordinate system, such as the robot's base (F_B).

While it is possible to measure the rotation angles and translation offsets between the scanner and flange manually, using for instance calipers, higher accuracy may be achieved using the positioner's and sensor's data. Solutions have been presented for hand-eye calibration for various equipment configurations [13-21]. We may classify those as either specimen-based, where a geometrically known physical object is used to assist in determining the missing transformation parameters using samples acquired from different poses [16,18,19]; and externally assisted methods, where additional sensing instruments are used to measure the relationship between the positioner and the scanner [20, 21]. Higher accuracy may be achieved using external measuring devices [20,22–25]. Nevertheless, specimen-based approaches, including the one presented here, are highly popular for being less costly and simple to perform regularly [26,27]. The challenge of calibrating profile scanners is in the missing spatial information given $y_s = 0$.

Relevant literature on profile sensor calibration methods uses various specimen geometries such as flat planes [13-15], circular disks

* Corresponding author.
E-mail address: stylianosdritsas@sutd.edu.sg (S. Dritsas).

https://doi.org/10.1016/j.rcim.2021.102221
Received 23 November 2020; Received in revised form 9 July 2021; Accepted 10 July 2021
Available online 30 July 2021

[16], spheres [17-19], blocks [21], and cross-hair targets [28,29]. Comparatively, these methods vary in the degree of manual effort and operator's level of expertise required in acquiring data [19,29]; the preparatory work on scanner fixtures and/or the measurement environment setup in the presence of obstructions [28]; the size of the data sets required in terms of the number of robot poses [4,14]; the precision and cost associated with the measured specimens [16,18,19]; and the complexity of the mathematical formulation recovering rotation and translation combined [13,14] or separately [12,30,31], using linear [13,14,28] versus non-linear [25,32], analytical [33] or iterative methods [13,14].

In this article, we propose a novel hand-eye calibration approach for profile sensors. Its geometric concept is based on sampling points from a straight edge, under various robot poses, and exploiting the implied co-linearity relationships to form systems of equations to recover the scanner's rotation and translation. There are several benefits in this approach: It does not require laborious sampling regimes and it is less amenable to human error, as the operator only needs to ensure that the laser line crosses the edge, as opposed to, methods requiring the operator to visually ensure the laser is passing exactly at the apex of a tapered pin, the center of a sphere or that it aligns with a crosshair target. It does not also require extremely precise or costly specimens; we demonstrate this by comparing precision-made artifacts with everyday common objects. It is conceptually simple, because we are working directly with observable features, namely edges, as opposed to plane normals and sphere centers. Finally, the mathematical formulation presented is based on elementary geometry concepts and linear regression techniques which may be efficiently implemented and solved.

2. Theoretical background

In line with relevant literature, we use homogenous $\mathscr{R}^{4\times4}$ transformation matrices to concisely express rotations and translations. We assume the world coordinate system coincides with the robot's base coordinate system, expressed as the identity matrix. Calibration aims at computing the scanner's rotation matrix $R_S \in \mathscr{R}^{3\times3}$ and translation vector $T_S \in \mathscr{R}^3$, with respect to the robot's flange $R_b \in \mathscr{R}^{3\times3}$ and $T_b \in \mathscr{R}^3$. The robot's pose is directly controllable, thus the flange coordinate system R_b, T_b with respect to the robot's base is known. Profile points $p_s : [x_s,\ 0,\ z_s]$ acquired from the scanner are also known, with respect to the unknown scanner's coordinate system R_s, T_s. Finally, profile positions $p_b : [x_b,\ y_b,\ z_b]$ with respect to the robot's base are also unknown (see Fig. 2). These relationships are expressed in homogenous

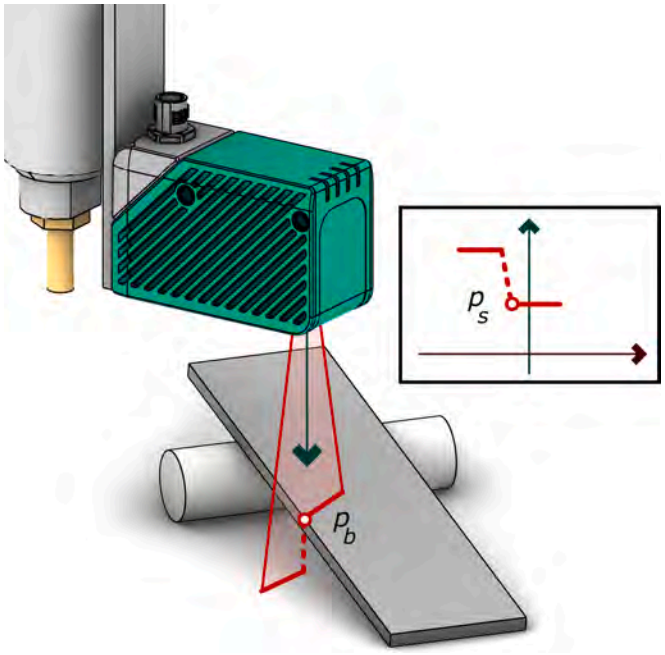

Fig. 2. Detail view of profile acquired from rectangular specimen and correspondence between feature point from edge detection with respect to the robot base coordinate space and the same point in the scanner coordinate space.

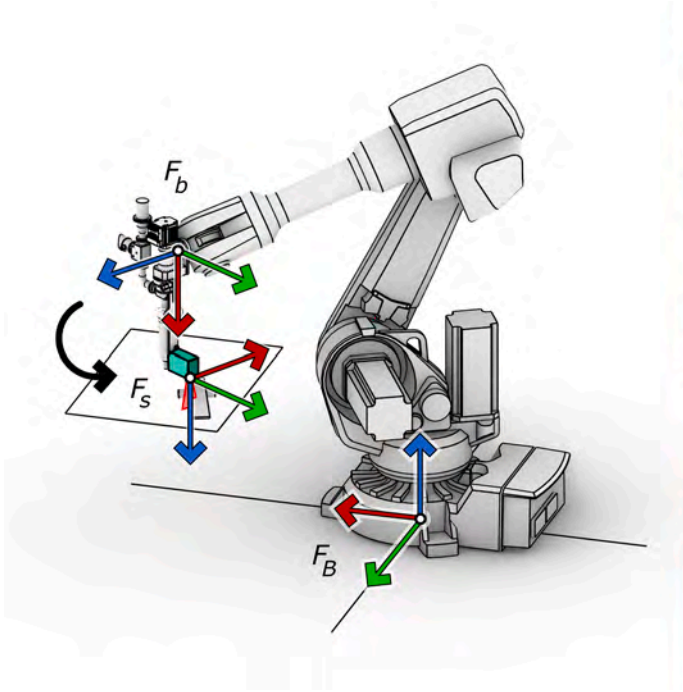

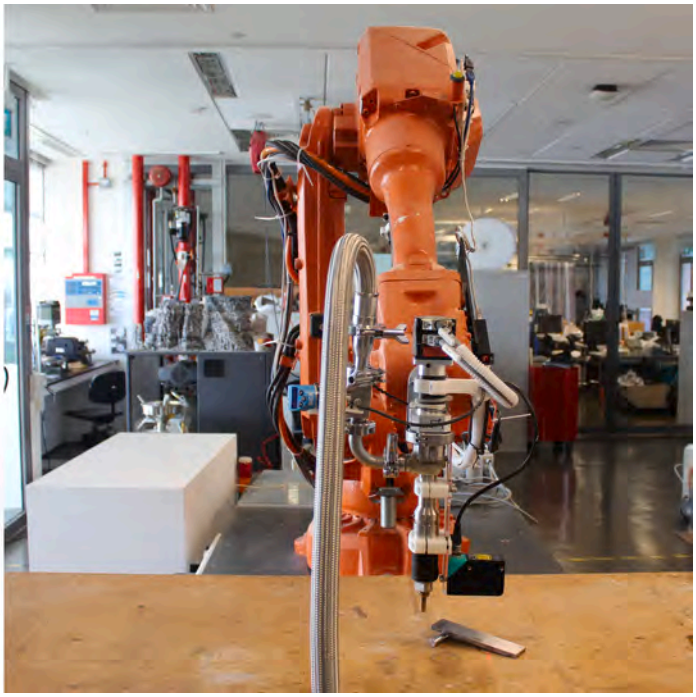

Fig. 1. An industrial robot with a 2D profile scanner (cyan). F_B represents the robot base coordinate system, F_b is the robot flange coordinate expressed in relation to F_B; and F_S is the scanner coordinate system. The objective of hand-eye calibration is to recover the transformation between F_b and F_S such that profiles scanned can be registered against F_B. The rotation and translation between F_b and F_S are R_S, T_S, respectively.

coordinates (Eq. 1), which states that the same point may be directly expressed with respect to the robot's base coordinate system (LHS) or as the product of a transformation from the robot's flange to the profile scanner's coordinate system (RHS).

$$\begin{bmatrix} p_b \\ 1 \end{bmatrix} = \begin{bmatrix} R_b & T_b \\ 0 & 1 \end{bmatrix} \cdot \begin{bmatrix} R_s & T_s \\ 0 & 1 \end{bmatrix} \cdot \begin{bmatrix} p_s \\ 1 \end{bmatrix} \tag{1}$$

We offer a sketch of the geometric logic before delving into the algebraic details. From a straight edge specimen, we extract multiple profile discontinuity feature points by sampling the specimen under different robot poses. Sampling follows a grid-like pattern, where rows and columns represent varying the robot's flange rotation and translation. Keeping the flange's rotation constant and varying translation, allows us to algebraically eliminate the scanner's translation component and derive equations for its rotation. However, we need multiple flange orientations to recover scanner's rotation, resulting into stacks of those equations. We recover the scanner's translation by using equations expressing the constraint that all points' distances to the linear edge must be notionally zero. In the presence of various sources of error, namely the robot, the scanner and the specimen, we approach recovery in a least-squares sense.

2.1. Recovering the rotation

We collect a series of profiles by translating the robot's flange, varying T_b, while retaining the robot's orientation R_b constant (see Fig. 3 left). Next, we extract feature points $p_{[1]}, p_{[2]}, \ldots p_{[n]}$ from each profile. Feature points in the scanner's coordinate system are expressed as $p_{s[1]}$, $p_{s[2]}$, $\ldots p_{s[n]}$, with the equivalent in robot's base coordinate system expressed as $p_{b[1]}, p_{b[2]}, \ldots p_{b[n]}$. We may rewrite equation (1), noting that the only varying quantities under these conditions are p_b, p_s, and T_b with a series of profiles under fixed flange orientation.

$$p_b = R_b(R_s p_s + T_s) + T_b \tag{2}$$

A first step towards eliminating unknown points from equation (1) is achieved by forming vectors from the first feature point $p_{[1]}$ to all others $p_{[2]}, p_{[3]}, \ldots p_{[n]}$. A vector, from points $p_{b[1]}$ to $p_{b[i]}$, where $i > 1$, with respect to the robot's base, is expressed as $u_{b[i]} = p_{b[i]} - p_{b[1]}$. Expanding this using Eq. (2) allows us to eliminate the scanner's translation component T_S, as shown in Eqs. (3, 4), and obtain Eq. (5) where $u_{s[i]}$ represents the edge's direction in the scanner's coordinate system and $u_{t[i]}$ represents the known robot's motion vector with respect to the robot's base.

$$u_{b[i]} = R_b(R_s p_{s[i]} + T_s) + T_{b[i]} - R_b(R_s p_{s[1]} + T_s) - T_{b[1]} \tag{3}$$

$$u_{b[i]} = R_b R_s p_{s[i]} - R_b R_s p_{s[1]} + T_{b[i]} - T_{b[1]} \tag{4}$$

$$u_{b[i]} = R_b R_s u_{s[i]} + u_{t[i]} \tag{5}$$

The second step towards deriving computable expressions, considers two different such directions $u_{b[i]}$ and $u_{b[j]}$; we thus need at least three samples per rotation set. Both originating from the same straight edge in physical space, allows us to express their parallelism as $\| u_{b[i]} \times u_{b[j]} \| = 0$. Using the rotational invariance of the cross product and expanding Eq. (6) produces:

$$\| (R_b R_s u_{s[i]} + u_{t[i]}) \times \left(R_b R_s u_{s[j]} + u_{t[j]}\right) \| = 0 \tag{6}$$

$$\| R_b R_s u_{s[i]} \times R_b R_s u_{s[j]} + R_b R_s u_{s[i]} \times u_{t[j]} - R_b R_s u_{s[j]} \times u_{t[i]} + u_{t[i]} \times u_{t[j]} \| = 0 \tag{7}$$

$$\| R_b R_s \left(u_{s[i]} \times u_{s[j]}\right) + R_b R_s u_{s[i]} \times u_{t[j]} - R_b R_s u_{s[j]} \times u_{t[i]} + u_{t[i]} \times u_{t[j]} \| = 0 \tag{8}$$

We may rewrite the first three parts of Eq. (8) to isolate the scanner's rotation R_s matrix, using matrix vectorization $r_s = vec(R_s)$ and the Kronecker product, denoted with $\otimes$.

$$R_b R_s \left(u_{s[i]} \times u_{s[j]}\right) = \left(\left(u_{s[i]} \times u_{s[j]}\right)^T \otimes R_b\right) r_s \tag{9}$$

$$R_b R_s u_{s[i]} = \left(\left(u_{s[i]}\right)^T \otimes R_b\right) r_s \tag{10}$$

$$R_b R_s u_{s[j]} = \left(\left(u_{s[j]}\right)^T \otimes R_b\right) r_s \tag{11}$$

Applying (9-11) to Eq. (8) produces Eq. (12). Note that the substituted terms (13-16), listed for clarity, capture known quantities, namely vectors from scanned points, the robot's flange rotation and the cross product of motion vectors.

$$\| B_1 r_s + B_2 r_s \times u_{t[j]} - B_3 r_s \times u_{t[i]} - b_r \| = 0 \tag{12}$$

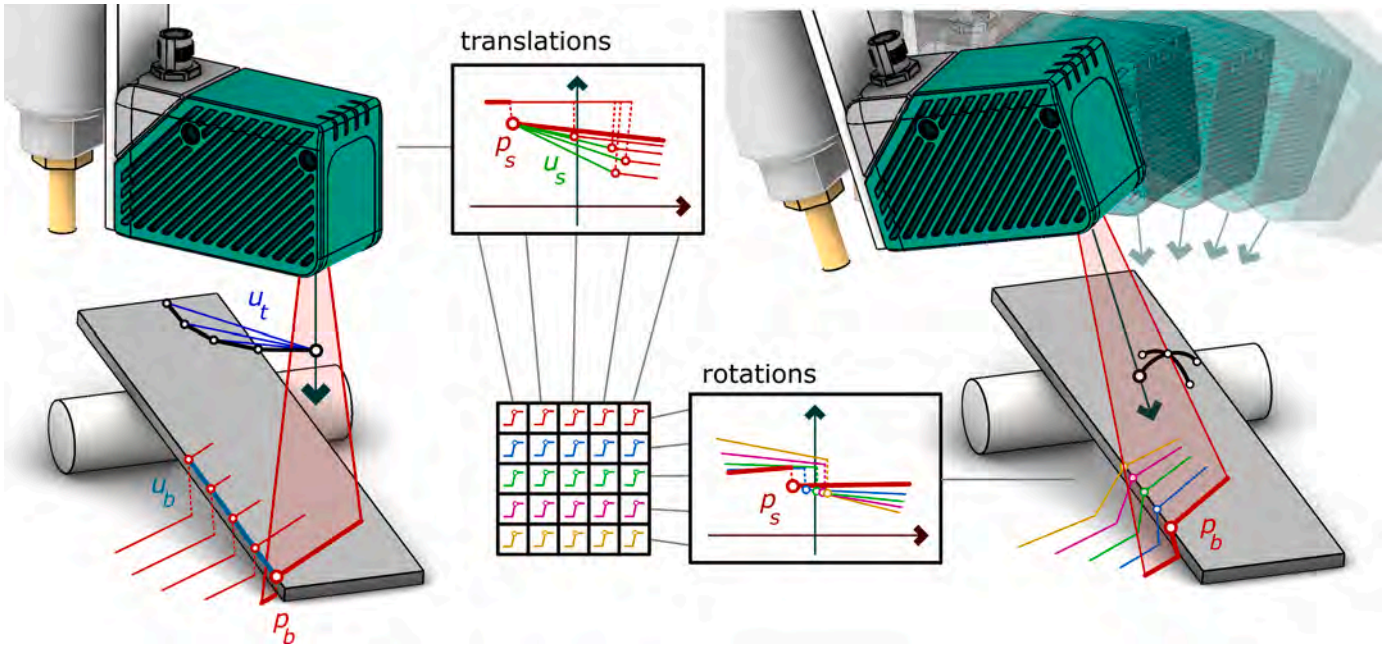

Fig. 3. Profiles of the same edge are collected from several robot poses and the edge feature points are extracted. Sampling follows a grid-like structure, where rows and columns represent varying the robot's flange translation and rotation.

$$B_1 = \left(\left(u_{s[i]} \times u_{s[j]}\right)^T \otimes R_b\right) \tag{13}$$

$$B_2 = \left(\left(u_{s[i]}\right)^T \otimes R_b\right) \tag{14}$$

$$B_3 = \left(\left(u_{s[j]}\right)^T \otimes R_b\right) \tag{15}$$

$$b_r = -u_{t[i]} \times u_{t[j]} \tag{16}$$

Using the skew-symmetric matrix form of the cross product (17), the motion vectors $u_{t[i]}$ and $u_{t[j]}$ are also brought into matrix-vector product form (18) and (19).

$$[a]_\times^T = \begin{bmatrix} 0 & a_3 & -a_2 \\ -a_3 & 0 & a_1 \\ a_2 & -a_1 & 0 \end{bmatrix} \tag{17}$$

$$B_2 r_s \times u_{t[j]} = \left[u_{t[j]}\right]_\times^T B_2 r_s \tag{18}$$

$$B_3 r_s \times u_{t[i]} = \left[u_{t[i]}\right]_\times^T B_3 r_s \tag{19}$$

Performing the cross-product to matrix substitutions to Eq. (12) produces the Eq. (20), with substitution terms (21-23) listed for clarity.

$$\| A_1 r_s + A_2 r_s - A_3 r_s - b_r \| = 0 \tag{20}$$

$$A_1 = B_1 \tag{21}$$

$$A_2 = \left[u_{t[j]}\right]_\times^T B_2 \tag{22}$$

$$A_3 = \left[u_{t[i]}\right]_\times^T B_3 \tag{23}$$

Factoring Eq. (20) and compounding data matrices, produces a desirable linear form (25) which may be solved in a least-squares sense. The *r* subscript denotes that these Eq.s are aimed to recover the rotation of the scanner's transformation matrix.

$$(A_1 + A_2 - A_3) r_s = b_r \tag{24}$$

$$A_r r_s = b_r \tag{25}$$

To obtain the scanner's rotation, we need to form an overdetermined system with a tall matrix A_r by stacking blocks of Eqs. (25), where each block represents sampling using a different flange rotation. The problem can now be approached in a least-squares regression sense using Eq. (26) to obtain $r_s^{'}$.

$$r_s^{'} = argmin \, \|A_r r_s - b_r\|^2 \tag{26}$$

We compute (26) using the Singular Value Decomposition (SVD) to obtain $r_s^{'} = V_1 S U_1^T b_r$. However, the matrix $R_s^{'}$ associated with the vector $r_s^{'}$, is not necessarily orthonormal and therefore not a valid rotation matrix. An orthonormal matrix in the nearest sense [34], R_s^* may be recovered using the SVD of matrix $R_s^{'}$, where $\det(U_2)\det(V_2)$ in the diagonal matrix is used to avoid improper rotations [31,35].

$$R_s^* = U_2 \begin{bmatrix} 1 & & \\ & 1 & \\ & & \det(U_2)\det(V_2) \end{bmatrix} V_2^T \tag{27}$$

2.2. Recovering the translation

With the rotation matrix R_s^* recovered, we compute the unit direction vector of the straight edge u_b^* in the robot's base coordinate system from Eq. (5) using Principal Components Analysis (PCA). For two points, $p_{b[i]}$ and $p_{b[j]}$ with respect to the robot's base coordinate system, sampled from different poses $R_{b[i]}$, $T_{b[i]}$ and $R_{b[j]}$, $T_{b[j]}$, their orthogonal Euclidean distance $\| (p_{b[j]} - p_{b[i]}) \times u_b^* \| = 0$ to the specimen's edge should be zero. Hence, expanding this distance using Eq. (2) and factoring relevant terms produces:

$$\| \left(R_{b[j]}\left(R_s^* p_{s[j]} + T_s\right) + T_{b[j]} - R_{b[i]}\left(R_s^* p_{s[i]} + T_s\right) - T_{b[i]}\right) \times u_b^* \| = 0 \tag{28}$$

$$\| \left(R_{b[j]} - R_{b[i]}\right) T_s \times u_b^* + \left(R_{b[j]} R_s^* p_{s[j]} - R_{b[i]} R_s^* p_{s[i]} + T_{b[j]} - T_{b[i]}\right) \times u_b^* \| = 0 \tag{29}$$

We may simplify Eq. (29) by substituting known quantities with more concise matrix-vector notation using the following substitutions:

$$\left(R_{b[j]} - R_{b[i]}\right) T_s \times u_b^* = C T_s \times u_b^* \tag{30}$$

$$-\left(R_{b[j]} R_s^* p_{s[j]} - R_{b[i]} R_s^* p_{s[i]} + T_{b[j]} - T_{b[i]}\right) \times u_b^* = b_t \tag{31}$$

Therefore, we produce Eq. (32) and proceed, as earlier, with replacing cross products with matrix-vector products. Again, we note that both matrix C and vector b_t capture known quantities, namely the robot's flange data and earlier computed values.

$$\| C T_s \times u_b^* - b_t \| = 0 \tag{32}$$

Simplifying Eq. (32), using the skew-symmetric matrix form of the cross product (17), produces the desired form of Eq. (34).

$$C T_s \times u_b^* = \left[u_b^*\right]_\times^T C T_s = A_t T_s \tag{33}$$

$$\| A_t T_s - b_t \| = 0 \tag{34}$$

By minimizing Eq. (34), we obtain T_s^*

$$T_s^* = argmin \, \|A_t T_s - b_t\|^2 \tag{35}$$

Obtaining the scanner's translation offsets is also approached in a least-squares sense by stacking Eqs. (34) using multiple pairs of poses as long as they don't belong to the same rotation group; to avoid canceling the scanner's translation (see Eq. 28). Finally, it also solved using the same SVD approach as the discussion in Section 2.1.

3. Instruments and experimental setup

The laboratory setup is comprised of an industrial articulated six-axis robot (ABB IRB2600) with 1.65m horizontal reach and 20kg payload, driven by the industrial controller (ABB IRC5). The ISO9283 pose accuracy of the robot is 0.03 mm with 0.04 mm pose repeatability. The profile scanner used (Pepperl+Fuchs VLM350-F280-R4-1101) has a measurement range of 40 to 160 mm and 60 to 350 mm, in the X and Z directions, respectively. Its specified resolution is X > 0.25 mm, Z > 0.2 mm at 60 mm distance. Its firmware reports at maximum 980 sample points per profile, quantized at 0.1 mm, encoded as 16-bit integers. No accuracy data is provided by the manufacturer. Measurement errors of edges by varying distance from the target are presented in the supplementary materials section. Experiments were conducted using various specimens including a machinist precision parallel bar with indicative accuracy of 0.01 mm, an engineering straight scale with a typical measurement accuracy of 0.1 mm, and a box cutter knife blade of unknown precision characteristics (see Fig. 4). Validation of the proposed method was performed using a precision ball with a 20mm radius and G10 sphericity as per ISO3290.

Measurements are characterized by errors attributed to the positional accuracy of the robot, the sensing accuracy of the scanner as well as the manufacturing tolerances of the specimens. The robot presents spatial errors across its work envelope result of its cantilevered structure and mechanical motor gearing. To minimize their influence, we performed calibration procedures as per the manufacturer's specification, restricted actions within a small work sub-space, and performed motions such that the axes are loaded. The profile scanner presents errors proportional to the distance to the specimen scanned. We planned motions within the range of 60 to 90 mm distance between the scanner and the specimens, for which the scanner performs best, according to the manufacturer's recommendations. The specimens were placed at an

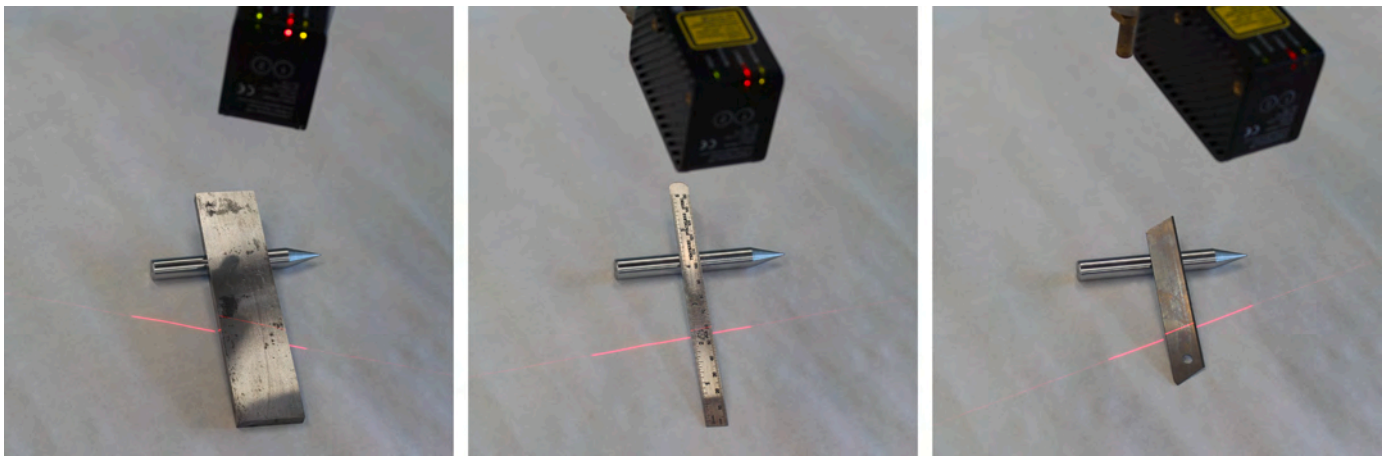

Fig. 4. Left: Machinist's precision ground parallel bar. Middle: Engineering straight scale. Right: Utility box-cutter knife blade.

arbitrary bias angle and an offset position against the robot's base and scanner's orientation to avoid singularities. The robot is jogged manually above the center of the specimen in approximately vertical direction. It was rotated manually to cover as large rotation angles as feasible within the constraint of the laser line crossing the same edge in the same sense. Translation motions follow a circular arc path. The arc's span angle and radius are input into the data acquisition script. The values used depend on the specimen's size, the robot's work envelope and the need to scan the same edge consistently with enough variation of all numerical data collected. Delays between motions were introduced to minimize the influence of robot vibrations, and to ensure the robot and scanner data are in sync. Vertical retraction and approach motions between poses were introduced to ensure the controller does not optimize away small motions. Feature point detection is directly supported by the scanner's firmware, but we implemented a filter between consecutive points of a profile to ensure the same was consistently used. For thin specimens, such as the box cutter's blade, feature point detection is automatic but for the machinist parallel bar, the side walls must be removed. Motion planning, scanner as well as flange data acquisition, communications and calibration model solving were performed using python and ABB Rapid programming. The program instructs the robot's motion and collects the data, therefore the process is quasi-automatic (see supplementary video).

4. Experimental context, results and discussion

The system's application context is quality control: to evaluate the shape of linear beads of adhesive material, approximately 12 mm in profile width by 3-4 mm in height, dispensed from the extruder mounted on the robot, on which the sensor is also mounted. The process aims at replacing manual 3D scanning, using an Artec MHT structured-light device with up to 0.5 mm resolution and 0.1 mm accuracy, using an integrated approach. Results that meet or improve the process are considered satisfactory.

We conducted a series of experiments using straight edges from three specimens of various precisions characteristics to understand their influence on calibration. Each of the straight edge specimens was scanned using 25 flange rotations by 10 translations. We also evaluated the number of samples used against their influence on the calibration results. Finally, we scanned a precision sphere to assess if we can match its radius and to verify the calibration, beyond analysis of the straight edge results.

4.1. Straight edge experiments

The calibration method has two phases, for each we introduce an error criterion. We use an angle deviation criterion $\Delta\alpha$ for the rotation recovery phase because we are working with vector quantities. Semantically, it captures the notion of the parallelism constraint. The criterion measures the fitness of alignment between the straight edge's direction obtained after performing principal components analysis, against the edge direction vectors estimated from each individual rotation group. The Euclidean distance criterion Δd, for the translation recovery phase, captures how well, feature points of sampled profiles, describe a common line in space, as a function of their projected distances onto it. Semantically this captures the co-linearity constraint (see Fig. 5). We executed the calibration process repeatedly by incrementally reducing the number of rotational poses used, from the maximum collected, in the order they were collected, to evaluate the change of errors in relationship to the number of samples. While limited within the original motion range domain, this approach offers insight in understanding how many poses may be sufficient.

The relationship between $\Delta\alpha$ and the number of scanning rotations for the three different calibration objects is shown in Fig. 6. At 15 rotations and greater, we observe that there is hardly any influence on $\Delta\alpha$. Based on this observation, we then only take into consideration the data obtained for 15, 20 and 25 rotations. Between this range of rotations, the absolute minimum and maximum $mean(\Delta\alpha)$ was 0.73° and 1.16°, and the minimum and maximum $std(\Delta\alpha)$ was 1.66° and 2.67°, as shown in Table 1.

The relationship between Δd and the number of scanning rotations for the three different calibration objects is shown in Fig. 7. Likewise, we observe that there is hardly any influence on Δd when the number of rotations is 15 and greater. Between 15, 20 and 25 rotations, the minimum and maximum $mean(\Delta d)$ was 0.22 mm and 0.31 mm, and the minimum and maximum $std(\Delta d)$ was 0.12 mm and 0.16 mm, as shown in Table 2.

From Table 1 and Table 2, we can observe that the influence of the three calibration objects is less than 0.1 mm, which demonstrates that the process is robust. Considering the sensor's and robot's limitations and the purposes of our application these deviations are also acceptable.

4.2. Sphere reconstruction experiment and results

Using the calibration parameters computed from the straight edge specimens, we performed a sphere reconstruction experiment to evaluate the method for 3D scanning suitability and to validate the calibration results. A precision steel ball with a 20 mm radius was fitted and its radius r was estimated, based on 60 profiles from 10 rotation groups of 6 translation profiles each (see Fig. 8).

The hand-eye calibration matrices, from the earlier section, were used to transform the profiles from 2D with respect to the scanner's

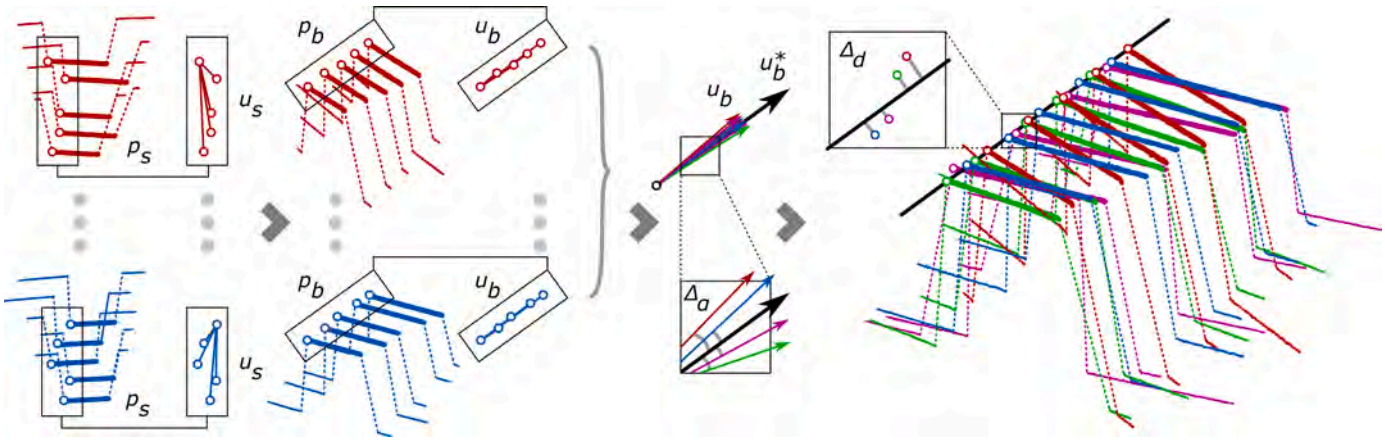

Fig. 5. Left-to-Right: Profiles are color-coded per robot's flange rotation. Their points form vectors from which the spatial edge direction is computed. The angle error represents rotation groups deviations from the spatial edge estimate. After translation is recovered, feature points distances from the spatial edge are used to compute the distance error criterion.

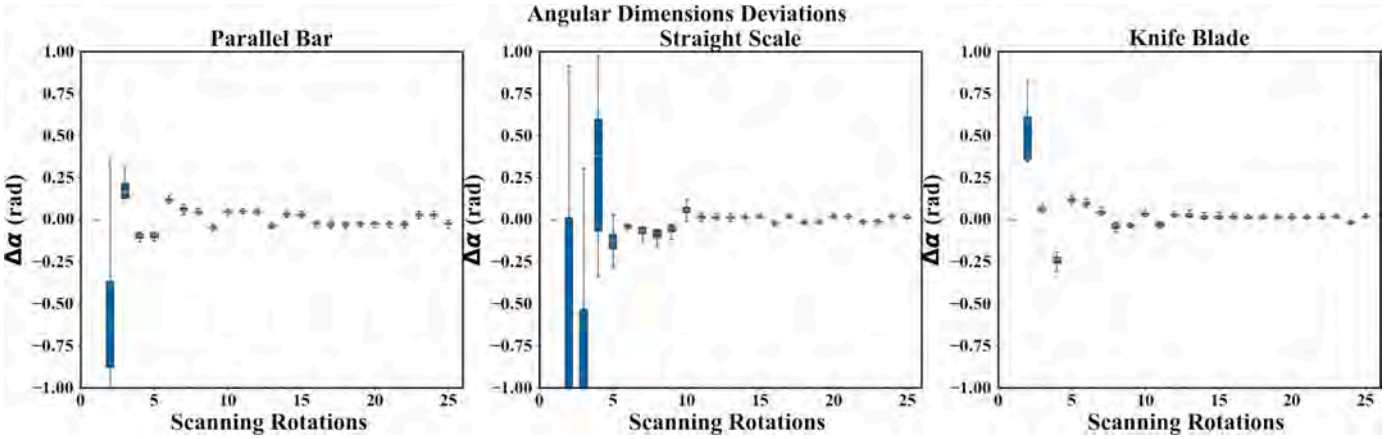

Fig. 6. The mean and standard angular dimensions' deviations ($\Delta\alpha$) of the first regression model.

Table 1
The mean and standard of $\Delta\alpha$ for 10, 15, 20, 25 scanning rotations.

Number of Rotations	*mean*($\Delta\alpha$) from Parallel Bar (°)	*std*($\Delta\alpha$) from Parallel Bar (°)	*mean*($\Delta\alpha$) from Straight Scale (°)	*std*($\Delta\alpha$) from Straight Scale (°)	*mean*($\Delta\alpha$) from Knife Blade (°)	*std*($\Delta\alpha$) from Knife Blade (°)
10	2.19	2.55	3.10	4.46	1.85	2.38
15	1.16	2.56	0.74	2.32	0.81	2.08
20	-1.03	2.67	0.86	1.95	0.84	1.74
25	-1.12	2.39	0.73	1.86	0.94	1.66

coordinate system, to 3D with respect to the robot's base coordinate system. Points of the sphere were extracted, and a sphere was fitted to the point-cloud using sphere regression [36]. The estimated radius results obtained are presented in Table 3, for each of the calibration specimens, with a varying number of rotations considered from 10 to 25. The minimum and maximum deviation of the estimated radius is in the range of 0.01 and 0.08 mm. The results show that the method is robust, and the accuracy of calibration is satisfactory for reconstruction.

5. Conclusion

A hand-eye calibration method for 2D profile laser scanners mounted on spatial positioners was presented. The theoretical basis of this straight edge-based approach was described, and experimental results were presented and discussed. The unique characteristic of this method is in its simplicity in both the sense of the regime of data acquisition as well as its mathematical formulation and computation. Straight edges are elementary in description, common to numerous manufactured products and detection thereof is 2D profile scanners' primary mode of operation. The experimental results for our application are satisfactory. Nevertheless, the method is general so profile sensors and positioners with better technical characteristics may achieve better results suit for purpose. The method may be improved by automating the data acquisition phase using incremental motions from the initial pose to infer the motion ranges. In a mathematical sense a more elegant single-phase derivation of the same concept may be possible using projective geometric algebra concepts [37,33,38].

CRediT authorship contribution statement

Jing Xu: Conceptualization, Methodology, Software, Validation, Visualization, Writing – original draft. **Jian Li Hoo:** Writing – review &

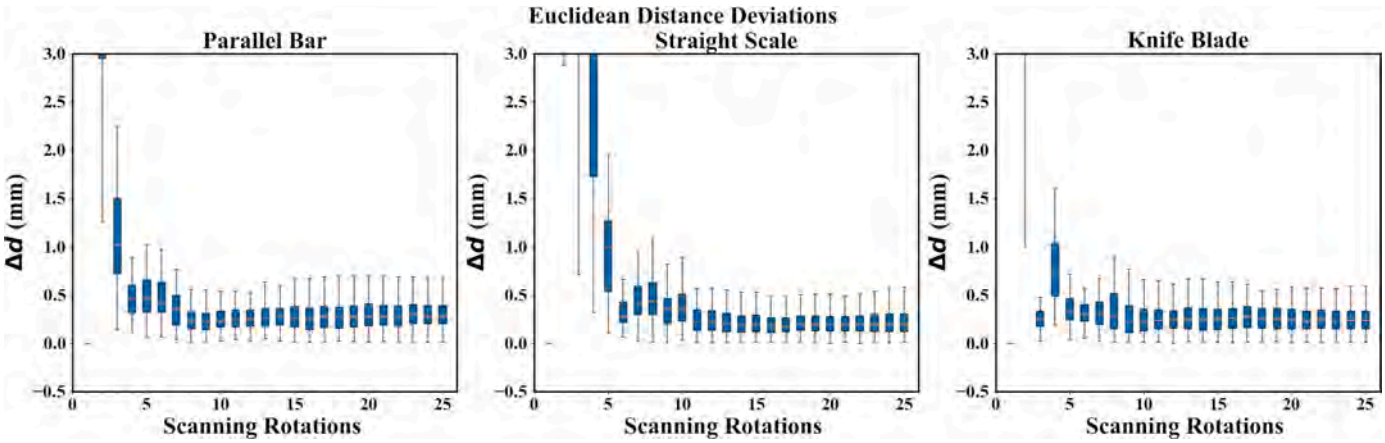

Fig. 7. The mean and standard deviations of the Euclidean distances (Δd) of the second regression model.

Table 2
The mean and standard deviations of Euclidean distances (Δd) for 10, 15, 20, 25 scanning rotations.

Number of Rotations	*mean*(Δd) from Parallel Bar (mm)	*std*(Δd) from Parallel Bar (mm)	*mean*(Δd) from Straight Scale (mm)	*std*(Δd) from Straight Scale (mm)	*mean*(Δd) from Knife Blade (mm)	*std*(Δd) from Knife Blade (mm)
10	0.27	0.16	0.37	0.19	0.27	0.17
15	0.28	0.15	0.22	0.12	0.26	0.14
20	0.30	0.16	0.22	0.14	0.26	0.14
25	0.31	0.16	0.23	0.15	0.25	0.14

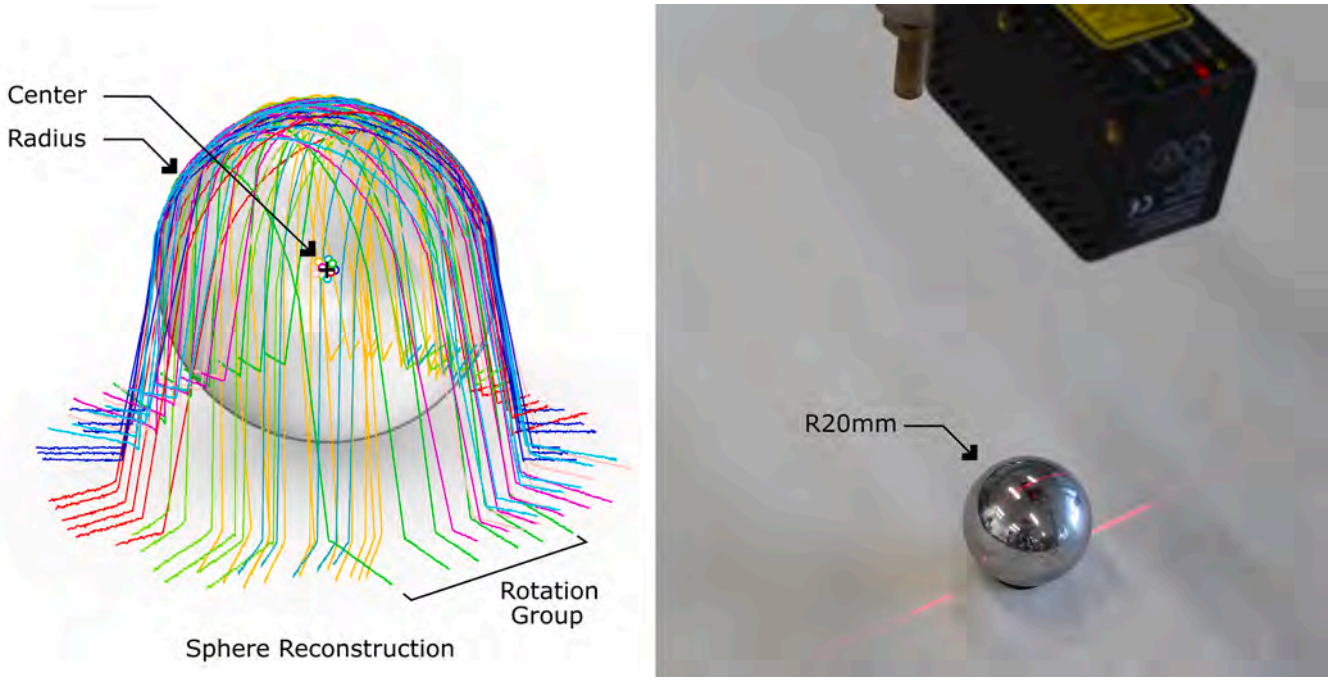

Fig. 8. Left: A sphere was fitted based on 10 groups of scanning rotations and 6 profile lines for each scanning rotation. Right: The laser sensor scanning a bearing steel ball with a 20 mm radius.

Table 3
The estimated radius (r) for 10, 15, 20, and 25 scanning rotations.

Number of Rotations	Parallel Bar (mm)	Straight Scale (mm)	Knife Blade (mm)
10	20.06	19.99	19.94
15	19.99	20.04	19.92
20	19.99	19.99	19.95
25	19.99	19.99	19.96

editing. **Stylianos Dritsas:** Project administration, Writing – review & editing. **Javier Gomez Fernandez:** Project administration, Writing – review & editing.

Declaration of Competing Interest

None.

Acknowledgements

This research has been supported by the Singaporean Ministry of Education through the MOE2018-T2-2-176 grant to JGF and SD.

Supplementary materials

Supplementary material associated with this article can be found, in the online version, at doi:10.1016/j.rcim.2021.102221.

References

[1] X Xu, D Zhu, H Zhang, S Yan, H. Ding, TCP-based calibration in robot-assisted belt grinding of aero-engine blades using scanner measurements, Int. J. Adv. Manuf. Technol. 90 (1) (2017) 635–647.
[2] S Sharifzadeh, I Biro, N Lohse, P. Kinnell, Robust surface abnormality detection for a robotic inspection system, IFAC-PapersOnLine 49 (21) (2016) 301–308.
[3] W-L Li, H Xie, G Zhang, S-J. Yan, Hand-eye calibration in visually-guided robot grinding, IEEE Trans. Cybernetics 46 (2015) 1–9.
[4] F Ernst, L Richter, L Matthaus, V Martens, R Bruder, A Schlaefer, et al., Non-orthogonal tool/flange and robot/world calibration, Int. J. Med. Robot 8 (4) (2012) 407–420.
[5] S Larsson, J. Kjellander, Motion control and data capturing for laser scanning with an industrial robot, Rob. Autom. Syst. 54 (6) (2006) 453–460.
[6] X Garcia-Cruz, OY Sergiyenko, V Tyrsa, M Rivas-Lopez, D Hernandez-Balbuena, J Rodriguez-Quiñonez, et al., Optimization of 3D laser scanning speed by use of combined variable step, Opt. Lasers Eng. 54 (2014) 141–151.
[7] L Lindner, O Sergiyenko, M Rivas-López, M Ivanov, JC Rodríguez-Quiñonez, D Hernández-Balbuena, et al., Machine vision system errors for unmanned aerial vehicle navigation, in: 2017 IEEE 26th International Symposium on Industrial Electronics (ISIE), IEEE, 2017.
[8] M Ivanov, O Sergiyenko, V Tyrsa, P Mercorelli, V Kartashov, W Hernandez, et al., Individual scans fusion in virtual knowledge base for navigation of mobile robotic group with 3D TVS, in: IECON 2018-44th Annual Conference of the IEEE Industrial Electronics Society, IEEE, 2018.
[9] D Lavrinov, A Khorkin, Problems of internal calibration of precision laser triangulation 2D scanners, in: 2016 2nd International Conference on Industrial Engineering, Applications and Manufacturing (ICIEAM), IEEE, 2016.
[10] H-L Huang, W-Y Jywe, C-H Liu, L Duan, M-S. Wang, Development of a novel laser-based measuring system for the thread profile of ballscrew, Opt. Lasers Eng. 48 (10) (2010) 1012–1018.
[11] J Rejc, J Činkelj, M. Munih, Dimensional measurements of a gray-iron object using a robot and a laser displacement sensor, Rob. Comput. Integr. Manuf. 25 (1) (2009) 155–167.
[12] K. Daniilidis, Hand-eye calibration using dual quaternions, Int. J. Robot. Res. 18 (3) (1999) 286–298.
[13] S Sharifzadeh, I Biro, P. Kinnell, Robust hand-eye calibration of 2D laser sensors using a single-plane calibration artefact, Rob. Comput. Integr. Manuf. 61 (2020), 101823.
[14] FB Carlson, R Johansson, A Robertsson, Six DOF eye-to-hand calibration from 2D measurements using planar constraints, in: 2015 IEEE/RSJ International Conference on Intelligent Robots and Systems (IROS), IEEE, 2015.
[15] M Li, Z Du, X Ma, W Dong, Y. Gao, A robot hand-eye calibration method of line laser sensor based on 3D reconstruction, Rob. Comput. Integr. Manuf. 71 (2021), 102136.
[16] W Chen, J Du, W Xiong, Y Wang, S Chia, B Liu, et al., A noise-tolerant algorithm for robot-sensor calibration using a planar disk of arbitrary 3-D orientation, IEEE Trans. Autom. Sci. Eng. 15 (1) (2018) 251–263.
[17] V Niola, C Rossi, S Savino, S. Strano, A method for the calibration of a 3-D laser scanner, Rob. Comput. Integr. Manuf. 27 (2011) 479–484.
[18] H Xie, C Pang, W Li, Y Li, Z Yin, Hand-eye calibration and its accuracy analysis in robotic grinding, in: 2015 IEEE International Conference on Automation Science and Engineering (CASE), 2015, 24-28 Aug. 2015.
[19] S Yin, Y Guo, Y Ren, J Zhu, S Yang, S. Ye, A novel TCF calibration method for robotic visual measurement system, Optik 125 (23) (2014) 6920–6925.
[20] J-S Hu, Y-J. Chang, Automatic calibration of hand–eye–workspace and camera using hand-mounted line laser, IEEE/ASME Trans. Mechatron. 18 (6) (2012) 1778–1786.
[21] J-S Hu, Y-J Chang, Calibration of an eye-to-hand system using a laser pointer on hand and planar constraints, in: 2011 IEEE International Conference on Robotics and Automation, IEEE, 2011.
[22] H Zhuang, SH Motaghedi, ZS Roth, Y. Bai, Calibration of multi-beam laser tracking systems, Robot. Comput. Integr. Manuf. 19 (2003) 301–314.
[23] A Nubiola, IA. Bonev, Absolute calibration of an ABB IRB 1600 robot using a laser tracker, Rob. Comput. Integr. Manuf. 29 (2013) 236–245.
[24] G Du, P Zhang, Li Di, Online robot calibration based on hybrid sensors using Kalman Filters, Rob. Comput. Integr. Manuf. 31 (2015) 91–100.
[25] GA Idrobo-Pizo, JMS Motta, RC. Sampaio, A calibration method for a laser triangulation scanner mounted on a robot arm for surface mapping, Sensors 19 (8) (2019) 1783.
[26] M Forsman, N Börlin, K Olofsson, H Reese, J. Holmgren, Bias of cylinder diameter estimation from ground-based laser scanners with different beam widths: a simulation study, ISPRS J. Photogramm. Remote Sens. 135 (2018) 84–92.
[27] FJ Brosed, JJ Aguilar, D Guillomía, J. Santolaria, 3D geometrical inspection of complex geometry parts using a novel laser triangulation sensor and a robot, Sensors 11 (1) (2011) 90–110.
[28] T Heikkilä, JM Ahola, J Koskinen, T Seppälä, Calibration procedures for object locating sensors in flexible robotized machining, in: 2014 IEEE/ASME 10th International Conference on Mechatronic and Embedded Systems and Applications (MESA), 2014, 10-12 Sept. 2014.
[29] S Yin, Y Ren, J Zhu, S Yang, S. Ye, A vision-based self-calibration method for robotic visual inspection systems, Sensors 13 (12) (2013) 16565–16582.
[30] J Wu, Y Sun, M Wang, M. Liu, Hand-eye calibration: 4-D procrustes analysis approach, IEEE Trans. Instrum. Meas. 69 (6) (2019) 2966–2981.
[31] KS Arun, TS Huang, SD. Blostein, Least-squares fitting of two 3-D point sets, IEEE Trans. Pattern Anal. Mach. Intell. (5) (1987) 698–700.
[32] C Yu, X Chen, J. Xi, Modeling and calibration of a novel one-mirror galvanometric laser scanner, Sensors 17 (1) (2017).
[33] D Condurache, A. Burlacu, Orthogonal dual tensor method for solving the AX= XB sensor calibration problem, Mech. Mach. Theory 104 (2016) 382–404.
[34] S Sarabandi, A Shabani, JM Porta, F. Thomas, On closed-form formulas for the 3-d nearest rotation matrix problem, IEEE Trans. Rob. 36 (4) (2020) 1333–1339.
[35] S. Umeyama, Least-squares estimation of transformation parameters between two point patterns, IEEE Trans. Pattern Anal. Mach. Intell. (4) (1991) 376–380.
[36] CF. Jekel, Obtaining Non-Linear Orthotropic Material Models for PVC-Coated Polyester via Inverse Bubble Inflation, Stellenbosch University, Stellenbosch, 2016.
[37] E Hitzer, T Nitta, Y. Kuroe, Applications of Clifford's geometric algebra, Adv. Appl. Clifford Algebras 23 (2) (2013) 377–404.
[38] D Hestenes, R. Ziegler, Projective geometry with Clifford algebra, Acta Appl. Math. 23 (1) (1991) 25–63.